

Article

Hybrid Molybdenum Carbide/Heteroatom-Doped Carbon Electrocatalyst for Advanced Oxygen Evolution Reaction in Hydrogen Production

Jihun Kim ¹, Dae Hoon Lee ², Yang Yang ³, Kai Chen ¹, Chunli Liu ⁴, Jun Kang ^{5,*} and Oi Lun Li ^{1,*}

¹ School of Materials Science and Engineering, Pusan National University, Busan 46241, Korea; happyengineer@pusan.ac.kr (J.K.); chenkai888@pusan.ac.kr (K.C.)

² Department of Plasma Engineering, Korean Institute of Machinery and Materials, Daejeon 34103, Korea; dhlee@kimm.re.kr

³ State Key Laboratory of Materials-Oriented Chemical Engineering, College of Chemical Engineering, Nanjing Tech University, Nanjing 211816, China; yangy@njtech.edu.cn

⁴ Department of Physics and Oxide Research Center, Hankuk University of Foreign Studies, Yongin 17035, Korea; chunliliu@hufs.ac.kr

⁵ Division of Marine Engineering, Korea Maritime and Ocean University, Busan 49112, Korea

* Correspondence: junkang@kmou.ac.kr (J.K.); helenali@pusan.ac.kr (O.L.L.)

Received: 5 August 2020; Accepted: 5 November 2020; Published: 8 November 2020



Abstract: Hydrogen energy is one of the key technologies that can help to prevent global warming. A water electrolysis process can be used to produce hydrogen, in which hydrogen is produced at one electrode of the electrochemical cell, and oxygen is produced at the other electrode. On the other hand, the oxygen evolution reaction (OER) requires multiple reaction steps and precious-metal-based catalysts (e.g., Ru/C, Ir/C, RuO₂, and IrO₂) as electrocatalysts to improve the reaction rate. Their high cost and limited supply, however, limit their applications to the mass production of hydrogen. In this study, boron, nitrogen-doped carbon incorporated with molybdenum carbide (MoC-BN/C) was synthesized to replace the precious-metal-based catalysts in the OER. B, N-doped carbon with nanosized molybdenum nanoparticles was fabricated by plasma engineering. The synthesized catalysts were heat-treated at 600, 700, and 800 °C in nitrogen for one hour to enhance the conductivity. The best MoC-BN/C electrocatalysts (heated at 800 °C) exhibited superior OER catalytic activity: 1.498 V (vs. RHE) and 1.550 V at a current density of 10 and 100 mA/cm², respectively. The hybrid electrocatalysts even outperformed the noble electrocatalyst (5 wt.% Ru/C) with higher stability. Therefore, the hybrid electrocatalyst can replace expensive precious-metal-based catalysts for the upcoming hydrogen economy.

Keywords: oxygen evolution reaction; hybrid electrocatalyst; hydrogen production; plasma engineering

1. Introduction

To prevent global warming, cars using hydrogen fuel cells, an eco-friendly technology, are expected to be on the market in the near future [1–3]. The development of technology for hydrogen fuel cells related directly to hydrogen fuel cell cars is very important, but the infrastructure for hydrogen production is needed. Currently, hydrogen is produced from the hydrocarbon reforming process, which is not a completely eco-friendly method and is undesirable from a long-term perspective [4]. On the other hand, water electrolysis, which produces hydrogen directly from water, is the most eco-friendly and desirable method [5]. In water electrolysis, the kinetics of the oxygen evolution

reaction (OER), which is a key step of water electrolysis, is sluggish and often requires electrocatalysts to reduce the overpotential from the thermodynamic potential of the reaction (1.23 V vs. RHE) [6]. Among these electrocatalysts for the OER, precious-metal-based catalysts, such as ruthenium (Ru)- and iridium (Ir)-based catalysts (e.g., Ru/C, Ir/C, RuO₂, and IrO₂), are benchmarks with highest catalytic activity in this reaction [7,8]. Nevertheless, the mass production of hydrogen using this method is still difficult because of the expensive and limited supply of precious metals [9].

Several cheaper alternative catalysts with metal phosphates, perovskites, chalcogenides, oxides/hydroxides, and phosphides are being developed as replacements for these precious-metal catalysts [6,10]. Carbon-based catalysts are alternative catalysts owing to the high electronic conductivity, low cost, and structural and morphological diversity of carbon [11]. Doping heteroatoms in the carbon matrix results in positive and negative charges because of electronegativity and atomic size differences. As a result, catalytically active sites can be produced to promote the reaction. These sites can result from both single-atom doping and co-doping [12–17]. Some studies suggested that boron–nitrogen-doped carbon has a remarkable electrochemical catalytic performance that can replace precious-metal catalysts. Sun et al. constructed a defective nanocarbon material doped with B and N as a bifunctional metal-free catalyst for the ORR and OER [18]. Huang et al. fabricated heteroatom (B, N) co-doped three-dimensional (3D) porous carbon with outstanding activity toward the ORR and improved OER performance to commercial Pt/C catalysts under alkaline conditions [19]. Jiang et al. examined B, N co-doped graphene as a catalyst in nonaqueous lithium-oxygen (Li-O₂) batteries [20]. Our group recently conducted a detailed study on B, N co-doped carbon. Based on the density functional theory (DFT) calculation, the OH molecule was firstly adsorbed on the top side of B atom in the B, N co-doped carbon, where the OH* chemisorption energy was more negative than that on N-doped carbon catalysts, which translated into a higher kinetic OER activity of B, N co-doped carbon [21].

Another way of producing cheaper alternative catalysts is employing transition metals (e.g., Ni, Fe, Co, Mn, W, and Mo) instead of noble metals (Ru, Ir, and Pt). The oxidation states of transition metals change easily (e.g., Ni^{2+/3+}, Co^{2+/3+}), and they are earth-abundant and relatively inexpensive [22]. Among these transition metals, molybdenum (Mo) has been adopted in several studies because of the versatile coordination in its highest valence state [23]. Regmi et al. employed nanocrystalline Mo₂C as a bifunctional water-splitting electrocatalyst with superior catalytic activity and electrochemical stability [24]. Kim et al. synthesized chemically coupled Co and Mo₂C nanoparticles, which showed that the Co surface coupled with Mo₂C was more electrophilic with higher affinity to OH⁻ than the bare Co surface [25]. Jiang et al. fabricated N-doped carbon encapsulating cobalt and molybdenum carbide nanoparticles that were highly active and showed long-term stability in hydrogen evolution reaction (HER) and OER processes [26]. Therefore, it was expected that there would be synergistic effects in the OER when molybdenum carbide and boron–nitrogen-doped carbon are combined chemically as an electrocatalyst.

If a catalyst studied in the laboratory is applied to real mass production, the economic efficiency and production speed should also be considered. In this study, plasma engineering was adopted, which allowed the catalysts to be synthesized in a short time at low temperatures and atmospheric pressures, and different from chemical vapor deposition (CVD) and annealing methods [27]. In addition to the already mentioned advantages, achieving the desired carbon bonding and doping the carbon matrix with heteroatoms is relatively simple, using this method depending on the precursors and electrodes. Previous studies reported the successful doping of heteroatoms (boron [28,29], nitrogen [30–32], halogen [33], and metal elements [34–36]) into carbon. Through this process, boron, nitrogen-doped carbon with molybdenum carbide (MoC-BN/C) was fabricated successfully and heated at various temperatures (600, 700, and 800 °C) to enhance the electroconductivity of the catalyst. Several analysis tests were conducted to examine the morphology and composition of the synthesized electrochemical catalysts at each heat-treatment temperature. The electrocatalytic performances of each sample and precious-metal catalyst (5 wt.% Ru/C) in OER were also compared.

2. Results and Discussion

2.1. Morphology and Physical Properties

Scanning electron microscopy (SEM) and transmission electron microscopy (TEM) were performed to observe the morphology of the MoC-BN/C samples (Figure 1). The particle size was relatively unaffected by the heat-treatment temperature. Approximately 20 nm spherical carbon nanoparticles were agglomerated with each other homogeneously (Figure 1a–d). In Figure 1e, the red circles indicate the molybdenum carbides of ~5 nm in the carbon matrix, where Figure 1f shows that the 20 nm carbon particle consists of several 5 nm carbon nanoballs. Energy dispersive X-ray spectroscopy (EDS) images of Figure S1 show that boron and nitrogen were doped uniformly into the carbon matrix, and molybdenum was also dispersed homogeneously.

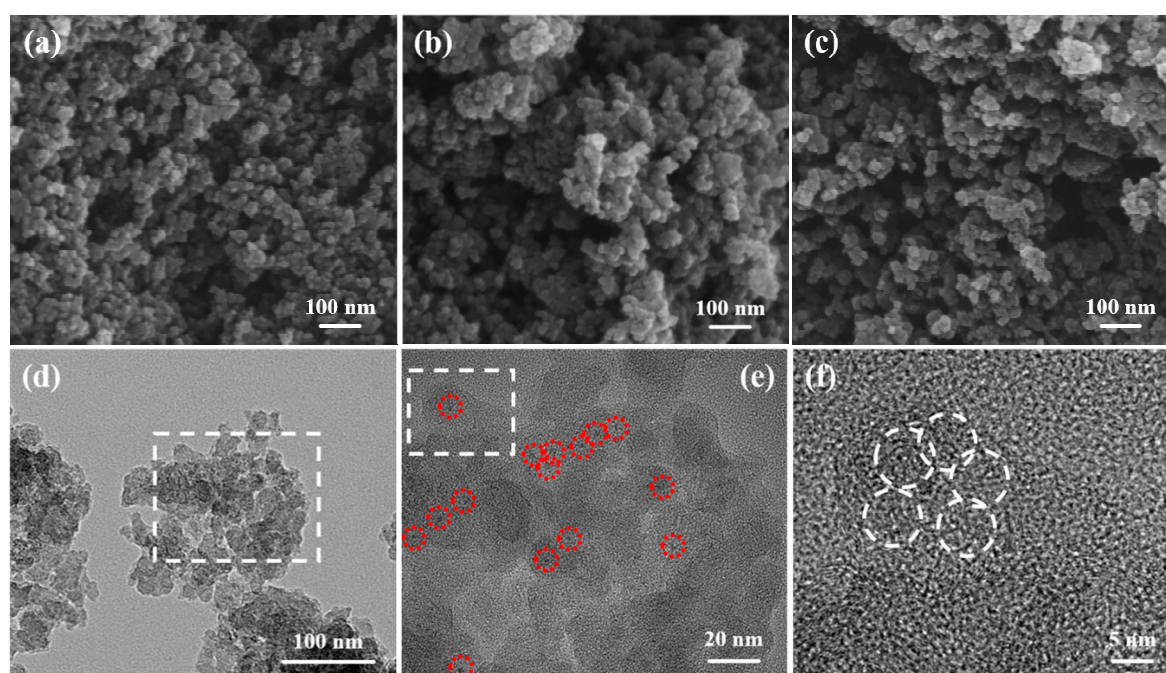


Figure 1. SEM images of (a) 600 MoC-BN/C, (b) 700 MoC-BN/C, and (c) 800 MoC-BN/C, (d) low-resolution TEM image of 800 MoC-BN/C, (e) and (f) high-resolution TEM images of 800 MoC-BN/C.

The same X-ray diffraction (XRD) peaks were observed in all catalysts (Figure 2a). The broad XRD peak at 23.4° was assigned to the (002) plane of graphitic carbon, highlighting the low crystallinity of the carbon. The XRD peaks at 36.4° , 42.2° , 61.4° , and 73.6° were attributed to the (111), (200), (220), and (311) planes for molybdenum carbide (MoC), respectively. Additionally, the Mo_2C peak was identified at 39.3° in only 800 MoC-BN/C. The crystallographic results confirmed that the MoC-BN/C catalysts consisted of the molybdenum carbide nanoparticles in the graphitic carbon support.

Using the Brunauer–Emmett–Teller (BET) method, the surface properties of the catalysts were investigated and are represented in Figure 2b,c and Table 1. As can be seen in the SEM and TEM images of Figure 1, all porosity in the catalysts occurred from interparticle voids. The N_2 adsorption–desorption isotherms of all samples showed Type-IV isotherms with H3 hysteresis loops. The hysteresis loops of high P/P_0 indicate that capillary condensation takes place in the mesopores [37]. The pore size distribution plots confirmed that most of the pores were made up of mesopores and macropores. With increasing heat-treatment temperature, the BET surface area increased, and 800 MoC-BN/C had the largest BET surface area with $295.16 \text{ m}^2/\text{g}$. In addition, the total pore volume and average

pore diameter decreased with increasing temperature due to the instability of grain structure and the pulverization of the crystal nucleus [38,39].

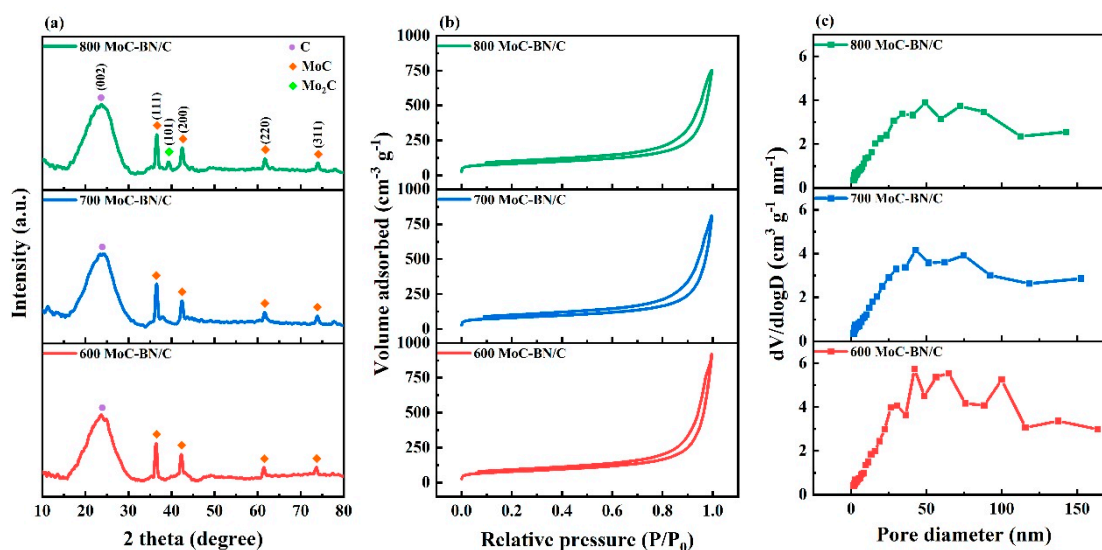


Figure 2. (a) XRD patterns of MoC-BN/C, (b) N₂ adsorption–desorption isotherm, (c) pore size distributions at the different heat-treatment temperatures.

Table 1. Surface properties of MoC-BN/C at different heat-treatment temperatures.

	600 MoC-BN/C	700 MoC-BN/C	800 MoC-BN/C
BET surface area	281.15 m ² /g	284.44 m ² /g	295.16 m ² /g
Total pore volume	1.34 cm ³ /g	1.16 cm ³ /g	1.09 cm ³ /g
Average pore diameter	11.751 nm	9.318 nm	9.231 nm

The chemical composition of 800 MoC-BN/C was identified by X-ray photoelectron spectroscopy (XPS) (Figure 3). Before the deconvolution of each peak, the XPS spectra were calibrated using the C 1s peak (~284.6 eV). Figure 3a shows that the C 1s was composed of four types of bonding: C–C (~284.6 eV), C–N (~285.4 eV), C–O (~286.7 eV), and C = O (~289.2 eV) [40]. In the C 1s spectrum, the C–C bonding was the most dominant peak. The N 1s spectrum was deconvoluted into pyridinic N (~399.0 eV), pyrrolic N (~400.4 eV), graphitic N (~401.7 eV), and oxidized N (~403.0 eV) [41,42]. These various bonding types were fabricated using quinoline as the precursor in plasma engineering. The B 1s spectrum was deconvoluted simply into two peaks: B–C (~189.0 eV) and B–N (~190.6 eV) [43,44]. In the B 1s spectrum, the B–C peak was higher than the B–N peak with showing the peak area ratio B–C: B–N = 1.47: 1. This means that most of the boron atoms were bonded with carbon atoms, but the number of boron atoms bonded with nitrogen atoms was also not little. Molybdenum can have various oxidation states. The Mo 3d peak could be deconvoluted into four peaks: Mo⁰ (~228.1 eV and ~231.6 eV), Mo³⁺ (~229.1 eV and ~232.9 eV), Mo⁴⁺ (~230.1 eV and ~234.9 eV), and Mo⁶⁺ (~232.3 eV and ~235.9 eV) [45,46]. The presence of especially high metallic molybdenum (Mo⁰) in 800 MoC-BN/C would be contributed to the high OER catalytic activity [23].

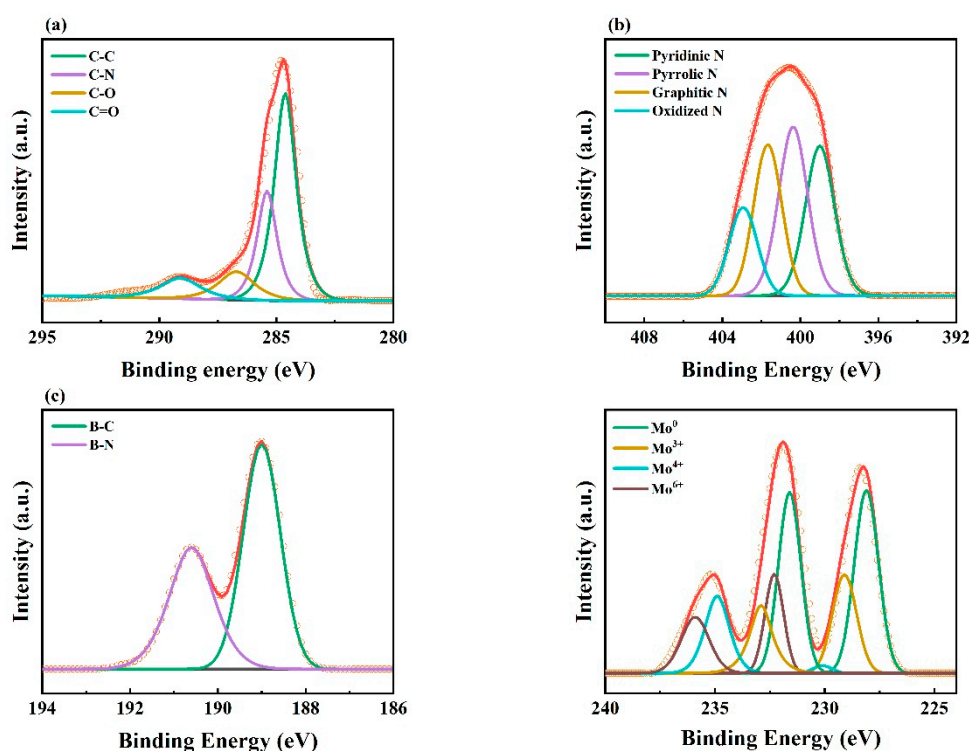
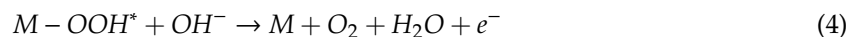
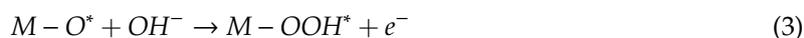
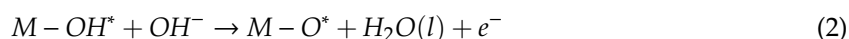


Figure 3. XPS spectra of 800 MoC-BN/C; (a) C 1s, (b) N 1s, (c) B 1s, and (d) Mo 3d.

2.2. Electrochemical Performances for the OER

The linear sweep voltammetry (LSV) method was used to evaluate the electrochemical catalysis activities in the OER (Figure 4a,b). 800 BN/C was fabricated by the same conditions with 800 MoC-BN/C except for using graphite electrodes instead of molybdenum electrodes during plasma engineering. From the comparison between 800 BN/C and 800 MoC-BN/C, it was confirmed that the addition of molybdenum carbides (MoC) into heteroatom-doped BN/C can boost the OER activity.

The OER mechanism in alkaline media is considered as follows:



where M represents a catalyst surface and * indicates an active site on the surface. In general, the OER process starts with the adsorption of the OH⁻ molecule on the catalyst. Based on DFT calculation, the B atom in the B, N-doped carbon matrix exhibits the more negative adsorption energy of OH* molecules and served as the major active site [21]. From our results, as shown in Figure 4a, the incorporation of MoC further enhances the OER activity of B, N-doped carbon, which might be accounted for further lowering the OH* adsorption energy via the synergic effect between MoC and B active sites. At a current density of 10 mA/cm², 5 wt.% Ru/C of the benchmark for the OER showed the lowest overpotential with 267 mV, but the difference with 800 MoC-BN/C was only 1 mV. Even at 50 and 100 mA/cm², 800 MoC-BN/C had the lowest overpotential with 305 mV and 320 mV, respectively. In addition, the overpotentials of the MoC-BN/C catalysts decreased with increasing heat-treatment temperature and showed lower overpotentials than 5 wt.% Ru/C except for 10 mA/cm². This was attributed to the enhanced electroconductivity by desorbing the hydrogen from the carbon lattice and forming of sp²-bonded carbon [47]. The mass activity of 800 MoC-BN/C was 5.46 mA/mg at 1.53 V

(vs. RHE) and showed the highest mass activity compared with other catalysts. The mass activity of 600 and 700 MoC-BN/C showed 4.14 and 4.49 mA/mg, and it was higher than that of 5 wt.% Ru/C (3.12 mA/mg).

The kinetic properties during the OER process were identified through a Tafel plot (Figure 4c). The 800 MoC-BN/C showed the lowest Tafel slope value, 50.7 mV/dec. This means that the lowest overpotential is needed to achieve the required current density at 800 MoC-BN/C among the catalysts. This linear tendency would be related to the increasing BET surface area with heat-treatment temperature.

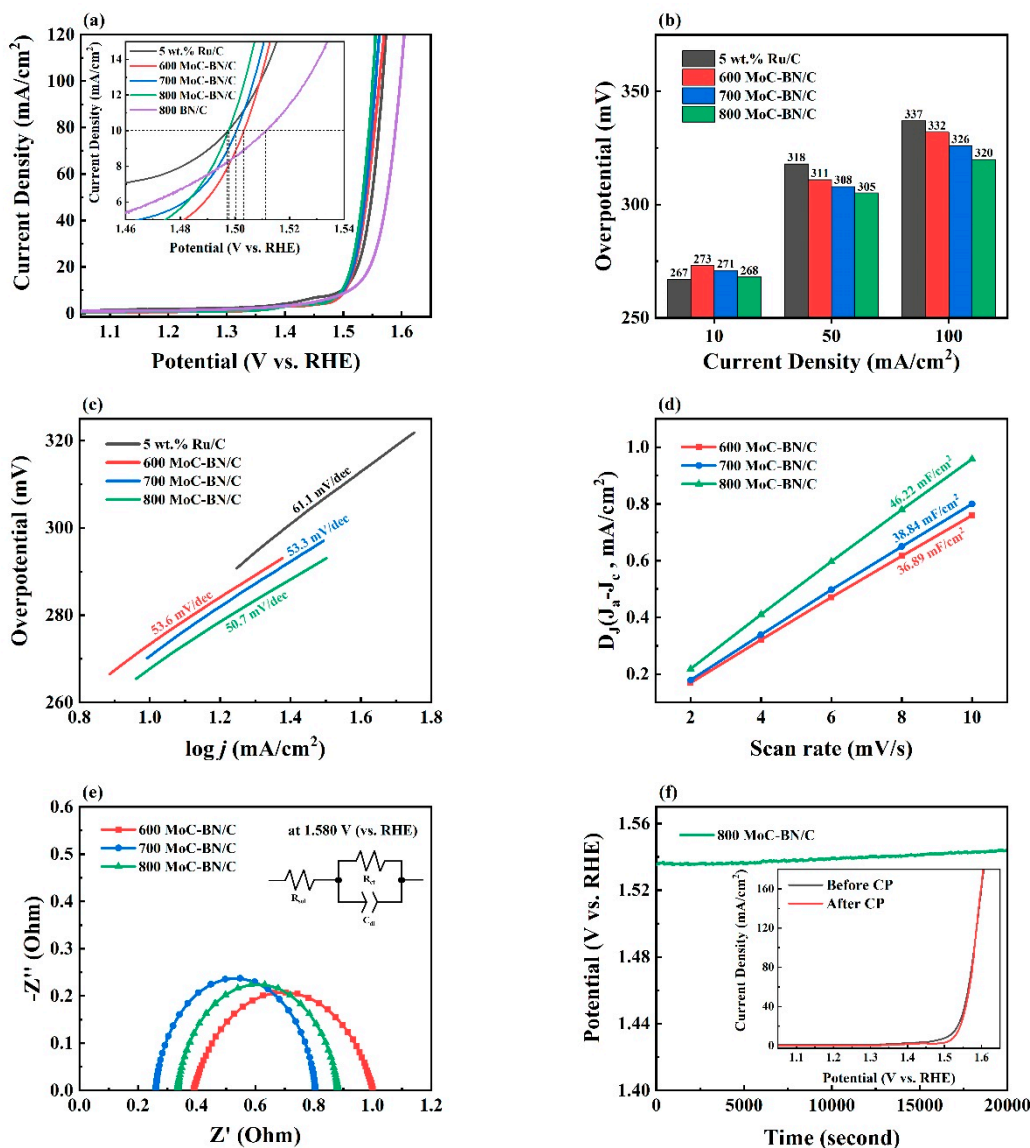


Figure 4. (a) Linear sweep voltammetry (LSV) curve of MoC-BN/C at 5 mV/s in N_2 saturated 1M KOH, (b) overpotential at 10, 50, and 100 mA/cm² for OER, (c) correlated Tafel slope from each LSV curve, (d) plotted graph at 0.99 V (vs. RHE) from cyclic voltammetry (CV) graphs conducted with several scan rates, (e) Nyquist plots obtained by electrochemical impedance spectroscopy (EIS) at 1.580 V (vs. RHE), and (f) chronopotentiometry (CP) curve of 800 MoC-BN/C at 10 mA/cm² for 20,000 s.

The cyclic voltammetry (CV) method with variable scan rates was carried out to identify the electrochemically active surface area (ECSA) of the MoC-BN/C catalysts in a non-faradaic region 0.94~1.04 V (vs. RHE) (Figure S3). ECSA was compared simply with C_{dl} (electrochemical double-layer

capacitance), which was calculated by dividing the linear slope of the capacitive current versus scan rate by two [48]. The C_{dl} values of each electrocatalyst were 36.89, 38.84, and 46.22 mF/cm² for 600, 700, and 800 MoC-BN/C, respectively. This linear tendency would be related to the increasing BET surface area with heat-treatment temperature [49] and was attributed to the enhanced probability of the occurrence of OER.

The charge transfer resistance (R_{ct}) of the MoC-BN/C catalysts was measured using the electrochemical impedance spectroscopy (EIS) method with the Nyquist plot at 1.580 V (vs. RHE), in which the OER was proceeded (Figure 4e). The Nyquist plots were fitted using a simple equivalent circuit, as shown in the figure [50]. Each semicircle is presented to the R_{ct} during the OER process. The R_{ct} value of 700 and 800 MoC-BN/C was the same with 0.54 Ω . In the case of 600 MoC-BN/C, the R_{ct} was 0.60 Ω .

The durability of 800 MoC-BN/C catalyst, which has the best activity among the synthesized catalysts, was tested using the chronopotentiometry (CP) method at 10 mA/cm² for 20,000 s (Figure 4f). At 10 s of CP, the potential was 1.535 V (vs. RHE). After 20,000 s, the potential increased by only 9 mV. Even in the LSV curves, after CP, a slightly lower overpotential was observed at a high current density.

By comparing the SEM images of 800 MoC-BN/C before (Figure 1c) and after OER (Figure 5a), it was confirmed that there was a little agglomeration, but the morphology remained almost unchanged. This showed that the catalyst has excellent stability. For comparison of the crystal structure change after the durability test, XRD analysis was conducted with the CP tested 800 MoC-BN/C powder. There were several peaks except for the original 800 MoC-BN/C peaks due to slurry components, electrolyte, and nickel foam. The XRD peaks at 24.2°, 30.0°, and 33.9° were attributed to the (110), (111), and (200) planes for potassium of 1M KOH electrolyte, respectively. In addition, the KO₂ peak at 31.3° mostly results from the electrolyte. The Ni peak at 44.4° occurred from nickel foam used as an electrode. The XRD pattern also showed other peaks aside from 800 MoC-BN/C peaks, but from maintaining 800 MoC-BN/C peak shape, it could be seen that there is little structural change in the catalyst after the OER.

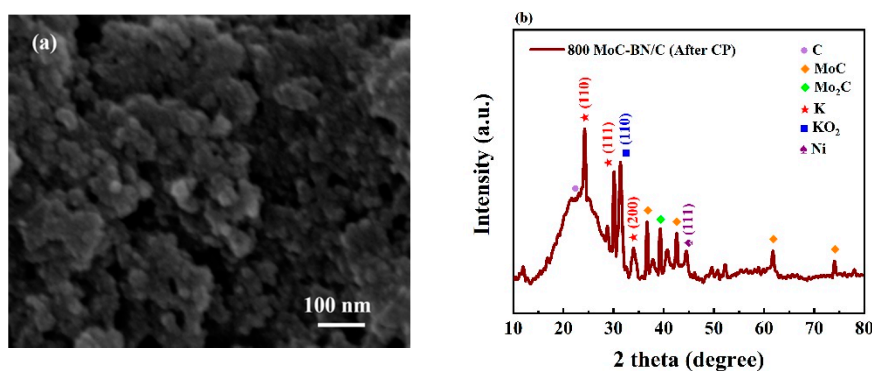


Figure 5. (a) SEM image of 800 MoC-BN/C after OER, (b) XRD pattern of 800 MoC-BN/C after OER.

3. Materials and Methods

3.1. Synthesis of MoC-BN/C by Plasma Engineering

As precursors of the plasma engineering, quinoline (purity > 95 %, Junsei Chemical, Tokyo, Japan) and boric acid (purity > 99.5 %, Junsei Chemical, Tokyo, Japan) were mixed using a homogenizer (Ultrasonic wave PZT vibrator, KSC-80, Korea Process Technology, Seoul, South Korea) for 3 h at 20 V. The boric acid was dissolved in 50 mL quinoline for 10 mM concentration. Molybdenum wire (Nilaco, Tokyo, Japan, 1.5 mm diameter) was used for the solution plasma electrodes. The plasma was discharged for 30 min at 4 kV at 50 kHz, and a pulse width of 0.8 μ s to synthesize the MoC-BN/C catalysts (Figure 6). After discharge, the solution was filtered with a polytetrafluoroethylene filter paper (diameter 55 mm, pore size 0.45 μ m), and the filtered sample was dried in an oven for one day at

80 °C. The dried sample was ground to a powder, and the sample was heated at 600, 700, and 800 °C for 1 h in nitrogen gas to improve the electrical conductivity.

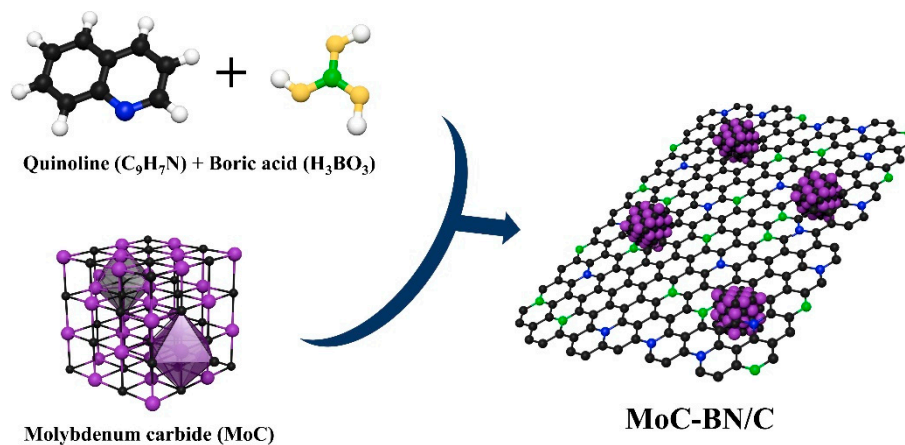


Figure 6. Schematic diagram of the synthesis of MoC-BN/C.

3.2. Material Characterization

Scanning electron microscopy (SEM, Supra 25, Zeiss, Oberkochen, Germany) and transmission electron microscopy (TEM, Talos F200X, FEI, Hillsboro, OR, USA) were used to observe the morphology of the fabricated powder. In TEM analysis, energy dispersive X-ray spectroscopy (EDS) was accompanied to analyze the chemical composition. X-ray diffraction (XRD, Xpert 3, Malvern Panalytical, Malvern, UK) was used to determine the crystal structure. The surface area, total pore volume, and pore size distribution were analyzed using the Brunauer–Emmett–Teller (BET, nanoPOROSITY-XQ, MiraeSI, Gwangju, South Korea) method. Chemical bonding and composition of the powder were characterized by X-ray photoelectron spectroscopy (XPS, AXIS Supra, Kratos Analytical, Manchester, UK).

3.3. Electrochemical Measurement

A potentiostat/galvanostat (VSP, Bio-Logic, Grenoble, France) was used to evaluate the electrochemical properties of the synthesized catalysts. The electrochemical test cell consisted of three electrodes. A Hg/HgO electrode (1M NaOH) and a spiral Pt wire electrode were used for the reference electrode and counter electrode, respectively. The working electrode was nickel foam (1 cm²) that had been coated with a slurry prepared by mixing 8 mg of the heat-treated MoC-BN/C powder, 1 mg of carbon nanotubes (Jeno tube 9, JEIO, Ansan, South Korea), 1 mg of poly(vinylidene fluoride) (average Mw~534,000 by GPC, Sigma-Aldrich, St. Louis, MO, USA), and 100 µL of 1-methyl-2-pyrrolidone (purity > 99.5 %, Samchun Chemicals, Seoul, South Korea). To compare the electrochemical property of MoC-BN/C catalysts, 5 wt.% Ru/C (Ruthenium on carbon-extent of labeling: 5 wt.% loading, Sigma-Aldrich, St. Louis, MO, USA) was used as a comparative catalyst, and the same amount with MoC-BN/C powder was loaded in order to make the slurry. Before the electrochemical measurements, 1M KOH solution was saturated with N₂ gas and used as the electrolyte. Linear sweep voltammetry (LSV) was performed at a scan rate of 5 mV/s to examine the OER activity of the electrochemical catalyst. From the LSV curve, the Tafel slope was calculated to compare the kinetics of the catalysts in the OER. The double-layer capacitance (C_{dl}) was calculated by cyclic voltammetry (CV) at various scan rates (2, 4, 6, 8, and 10 mV/s) in a non-faradaic region (0.94~1.04 V vs. RHE) to investigate the electrochemical surface area (ECSA) of the synthesized catalyst [51]. Electrochemical impedance spectroscopy (EIS) was conducted in potentiostatic mode at 1.580 V (vs. RHE), and the data was plotted on a Nyquist plot. The plotted semicircle is denoted as the charge-transfer resistance (R_{ct}) [52]. The stability of the catalyst was analyzed by chronopotentiometry (CP) at a current density of 10 mA/cm² for 20,000 s. Before and

after CP, LSV was performed to identify the change in catalytic activity. All potential values were converted to the reversible hydrogen electrode (RHE) with $E_{\text{RHE}} = E_{\text{Hg/HgO}} + (0.059 \times \text{pH}) + E^{\circ}_{\text{Hg/HgO}}$.

4. Conclusions

In summary, a hybrid molybdenum carbide/heteroatom-doped carbon electrocatalyst was fabricated successfully by a simple plasma engineering. To enhance the electroconductivity of the synthesized catalysts, heat-treatments were conducted at 600, 700, and 800 °C. The catalytic performance increased with increasing heat-treatment temperature. The 800 MoC-BN/C catalyst heat-treated at 800 °C showed the best catalytic performance in the OER. Although the overpotential of 800 MoC-BN/C (268 mV) was slightly higher than that of 5 wt.% Ru/C (267 mV), at a high current density (100 mA/cm²), the 800 MoC-BN/C (320 mV) surpassed 5 wt.% Ru/C (337 mV). In the CP test, 800 MoC-BN/C showed remarkable durability after 20,000 s at 10 mA/cm². Overall, 800 MoC-BN/C is an efficient and high-performed electrocatalyst for the OER.

Supplementary Materials: The following are available online at <http://www.mdpi.com/2073-4344/10/11/1290/s1>, Figure S1: EDS images of 800 MoC-BN/C in TEM; Figure S2: XRD pattern of 800 BN/C; Figure S3: CV graphs of 600, 700, and 800 MoC-BN/C to identify the electrochemically active surface area.

Author Contributions: Conceptualization, J.K. (Jun Kang) and O.L.L.; methodology, O.L.L. and D.H.L.; writing—original draft preparation, J.K. (Jihun Kim); writing—review and editing, Y.Y., C.L., K.C., and J.K. (Jihun Kim); supervision, J.K. (Jun Kang) and O.L.L.; funding acquisition, Y.Y. and D.H.L. All authors have read and agreed to the published version of the manuscript.

Funding: This research was funded by the Institutional program of KIMM (NK219E) and an open research grant (KL18-04) from the State Key Laboratory of Materials-Oriented Chemical Engineering, Nanjing Tech University, China.

Acknowledgments: The authors thank Seonghee Kim and Rajmohan Rajendiran for the valuable discussion.

Conflicts of Interest: The authors declare no conflict of interest.

References

1. Chen, L.-N.; Hou, K.-P.; Liu, Y.-S.; Qi, Z.-Y.; Zheng, Q.; Lu, Y.-H.; Chen, J.-Y.; Chen, J.-L.; Pao, C.-W.; Wang, S.-B. Efficient hydrogen production from methanol using a single-site Pt1/CeO2 catalyst. *J. Am. Chem. Soc.* **2019**, *141*, 17995–17999. [[CrossRef](#)] [[PubMed](#)]
2. Chandran, P.; Ghosh, A.; Ramaprabhu, S. High-performance Platinum-free oxygen reduction reaction and hydrogen oxidation reaction catalyst in polymer electrolyte membrane fuel cell. *Sci. Rep.* **2018**, *8*, 1–11. [[CrossRef](#)]
3. Pedersen, C.M.; Escudero-Escribano, M.; Velázquez-Palenzuela, A.; Christensen, L.H.; Chorkendorff, I.; Stephens, I.E. Benchmarking Pt-based electrocatalysts for low temperature fuel cell reactions with the rotating disk electrode: Oxygen reduction and hydrogen oxidation in the presence of CO. *Electrochim. Acta* **2015**, *179*, 647–657. [[CrossRef](#)]
4. Nwanebu, E.O.; Yao, Y.; Omanovic, S. The influence of Ir content in (Ni_{0.4}Co_{0.6})_{1-x}Ir_x-oxide anodes on their electrocatalytic activity in oxygen evolution by acidic and alkaline water electrolysis. *J. Electroanal. Chem.* **2020**, 114122. [[CrossRef](#)]
5. Yan, Y.; Xia, B.Y.; Zhao, B.; Wang, X. A review on noble-metal-free bifunctional heterogeneous catalysts for overall electrochemical water splitting. *J. Mater. Chem. A* **2016**, *4*, 17587–17603. [[CrossRef](#)]
6. Zhu, Y.; Zhou, W.; Chen, Z.G.; Chen, Y.; Su, C.; Tadé, M.O.; Shao, Z. SrNb_{0.1}Co_{0.7}Fe_{0.2}O_{3-δ} perovskite as a next-generation electrocatalyst for oxygen evolution in alkaline solution. *Angew. Chem.* **2015**, *127*, 3969–3973. [[CrossRef](#)]
7. Shinde, S.S.; Lee, C.-H.; Sami, A.; Kim, D.-H.; Lee, S.-U.; Lee, J.-H. Scalable 3-D carbon nitride sponge as an efficient metal-free bifunctional oxygen electrocatalyst for rechargeable Zn–air batteries. *ACS Nano* **2017**, *11*, 347–357. [[CrossRef](#)] [[PubMed](#)]
8. Lee, Y.; Suntivich, J.; May, K.J.; Perry, E.E.; Shao-Horn, Y. Synthesis and activities of rutile IrO₂ and RuO₂ nanoparticles for oxygen evolution in acid and alkaline solutions. *J. Phys. Chem. Lett.* **2012**, *3*, 399–404. [[CrossRef](#)] [[PubMed](#)]

9. Chen, C.-F.; King, G.; Dickerson, R.M.; Papin, P.A.; Gupta, S.; Kellogg, W.R.; Wu, G. Oxygen-deficient BaTiO_{3-x} perovskite as an efficient bifunctional oxygen electrocatalyst. *Nano Energy* **2015**, *13*, 423–432. [[CrossRef](#)]
10. Anjum, M.A.R.; Lee, M.H.; Lee, J.S. Boron-and nitrogen-codoped molybdenum carbide nanoparticles imbedded in a BCN network as a bifunctional electrocatalyst for hydrogen and oxygen evolution reactions. *ACS Catal.* **2018**, *8*, 8296–8305. [[CrossRef](#)]
11. Filimonenkov, I.S.; Bouillet, C.; Kéranguéven, G.; Simonov, P.A.; Tsirlina, G.A.; Savinova, E.R. Carbon materials as additives to the OER catalysts: RRDE study of carbon corrosion at high anodic potentials. *Electrochim. Acta* **2019**, *321*, 134657. [[CrossRef](#)]
12. Murdachaew, G.; Laasonen, K. Oxygen evolution reaction on nitrogen-doped defective carbon nanotubes and graphene. *J. Phys. Chem. C* **2018**, *122*, 25882–25892. [[CrossRef](#)]
13. Jiang, H.; Gu, J.; Zheng, X.; Liu, M.; Qiu, X.; Wang, L.; Li, W.; Chen, Z.; Ji, X.; Li, J. Defect-rich and ultrathin N doped carbon nanosheets as advanced trifunctional metal-free electrocatalysts for the ORR, OER and HER. *Energy Environ. Sci.* **2019**, *12*, 322–333. [[CrossRef](#)]
14. Gu, J.; Magagula, S.; Zhao, J.; Chen, Z. Boosting ORR/OER activity of graphdiyne by simple heteroatom doping. *Small Methods* **2019**, *3*, 1800550. [[CrossRef](#)]
15. Vineesh, T.V.; Kumar, M.P.; Takahashi, C.; Kalita, G.; Alwarappan, S.; Pattanayak, D.K.; Narayanan, T.N. Bifunctional electrocatalytic activity of boron-doped graphene derived from boron carbide. *Adv. Energy Mater.* **2015**, *5*, 1500658. [[CrossRef](#)]
16. Zhang, J.; Zhao, Z.; Xia, Z.; Dai, L. A metal-free bifunctional electrocatalyst for oxygen reduction and oxygen evolution reactions. *Nat. Nanotechnol.* **2015**, *10*, 444–452. [[CrossRef](#)]
17. El-Sawy, A.M.; Mosa, I.M.; Su, D.; Guild, C.J.; Khalid, S.; Joesten, R.; Rusling, J.F.; Suib, S.L. Controlling the active sites of sulfur-doped carbon nanotube–graphene nanolobes for highly efficient oxygen evolution and reduction catalysis. *Adv. Energy Mater.* **2016**, *6*, 1501966. [[CrossRef](#)]
18. Sun, T.; Wang, J.; Qiu, C.; Ling, X.; Tian, B.; Chen, W.; Su, C. B, N Codoped and Defect-Rich Nanocarbon Material as a Metal-Free Bifunctional Electrocatalyst for Oxygen Reduction and Evolution Reactions. *Adv. Sci.* **2018**, *5*, 1800036. [[CrossRef](#)]
19. Huang, X.; Wang, Q.; Jiang, D.; Huang, Y. Facile synthesis of B, N co-doped three-dimensional porous graphitic carbon toward oxygen reduction reaction and oxygen evolution reaction. *Catal. Commun.* **2017**, *100*, 89–92. [[CrossRef](#)]
20. Jiang, H.; Zhao, T.; Shi, L.; Tan, P.; An, L. First-principles study of nitrogen-, boron-doped graphene and co-doped graphene as the potential catalysts in nonaqueous Li–O₂ batteries. *J. Phys. Chem. C* **2016**, *120*, 6612–6618. [[CrossRef](#)]
21. Li, O.L.; Pham, N.N.; Kim, J.; Choi, H.; Lee, D.H.; Yang, Y.; Yao, W.; Cho, Y.-R.; Lee, S.G. Insights on boosting oxygen evolution reaction performance via boron incorporation into nitrogen-doped carbon electrocatalysts. *Appl. Surf. Sci.* **2020**, *528*, 146979. [[CrossRef](#)]
22. Cao, X.; Johnson, E.; Nath, M. Identifying high-efficiency oxygen evolution electrocatalysts from Co–Ni–Cu based selenides through combinatorial electrodeposition. *J. Mater. Chem. A* **2019**, *7*, 9877–9889. [[CrossRef](#)]
23. Liu, P.F.; Yang, S.; Zheng, L.R.; Zhang, B.; Yang, H.G. Mo 6+ activated multimetal oxygen-evolving catalysts. *Chem. Sci.* **2017**, *8*, 3484–3488. [[CrossRef](#)]
24. Regmi, Y.N.; Wan, C.; Duffee, K.D.; Leonard, B.M. Nanocrystalline Mo₂C as a bifunctional water splitting electrocatalyst. *ChemCatChem* **2015**, *7*, 3911–3915. [[CrossRef](#)]
25. Kim, M.; Kim, S.; Song, D.; Oh, S.; Chang, K.J.; Cho, E. Promotion of electrochemical oxygen evolution reaction by chemical coupling of cobalt to molybdenum carbide. *Appl. Catal. B* **2018**, *227*, 340–348. [[CrossRef](#)]
26. Jiang, J.; Liu, Q.; Zeng, C.; Ai, L. Cobalt/molybdenum carbide@ N-doped carbon as a bifunctional electrocatalyst for hydrogen and oxygen evolution reactions. *J. Mater. Chem. A* **2017**, *5*, 16929–16935. [[CrossRef](#)]
27. Morishita, T.; Ueno, T.; Panomsuwan, G.; Hieda, J.; Yoshida, A.; Bratescu, M.A.; Saito, N. Fastest formation routes of nanocarbons in solution plasma processes. *Sci. Rep.* **2016**, *6*, 36880. [[CrossRef](#)]
28. Panomsuwan, G.; Saito, N.; Ishizaki, T. Electrocatalytic oxygen reduction activity of boron-doped carbon nanoparticles synthesized via solution plasma process. *Electrochem. Commun.* **2015**, *59*, 81–85. [[CrossRef](#)]
29. Lee, S.-H. Solution Plasma Synthesis of BNC Nanocarbon for Oxygen Reduction Reaction. *J. Korean Inst. Surf. Eng.* **2018**, *51*, 332–336. [[CrossRef](#)]

30. Li, O.L.; Chiba, S.; Wada, Y.; Lee, H.; Ishizaki, T. Selective nitrogen bonding states in nitrogen-doped carbon via a solution plasma process for advanced oxygen reduction reaction. *RSC Adv.* **2016**, *6*, 109354–109360. [[CrossRef](#)]
31. Panomsuwan, G.; Chiba, S.; Kaneko, Y.; Saito, N.; Ishizaki, T. In situ solution plasma synthesis of nitrogen-doped carbon nanoparticles as metal-free electrocatalysts for the oxygen reduction reaction. *J. Mater. Chem. A* **2014**, *2*, 18677–18686. [[CrossRef](#)]
32. Hyun, K.; Saito, N. The solution plasma process for heteroatom-carbon nanosheets: The role of precursors. *Sci. Rep.* **2017**, *7*, 1–9. [[CrossRef](#)]
33. Ishizaki, T.; Wada, Y.; Chiba, S.; Kumagai, S.; Lee, H.; Serizawa, A.; Li, O.L.; Panomsuwan, G. Effects of halogen doping on nanocarbon catalysts synthesized by a solution plasma process for the oxygen reduction reaction. *Phys. Chem. Chem. Phys.* **2016**, *18*, 21843–21851. [[CrossRef](#)]
34. Kang, J.; Li, O.L.; Saito, N. A simple synthesis method for nano-metal catalyst supported on mesoporous carbon: The solution plasma process. *Nanoscale* **2013**, *5*, 6874–6882. [[CrossRef](#)]
35. Panomsuwan, G.; Chantaramethakul, J.; Chokradjaroen, C.; Ishizaki, T. In situ solution plasma synthesis of silver nanoparticles supported on nitrogen-doped carbons with enhanced oxygen reduction activity. *Mater. Lett.* **2019**, *251*, 135–139. [[CrossRef](#)]
36. Kim, S.; Park, H.; Li, O.L. Cobalt Nanoparticles on Plasma-Controlled Nitrogen-Doped Carbon as High-Performance ORR Electrocatalyst for Primary Zn-Air Battery. *Nanomaterials* **2020**, *10*, 223. [[CrossRef](#)]
37. Sing, K.S. Reporting physisorption data for gas/solid systems with special reference to the determination of surface area and porosity (Recommendations 1984). *Pure Appl. Chem.* **1985**, *57*, 603–619. [[CrossRef](#)]
38. Xu, Y.H.; Liu, Q.; Zhu, Y.J.; Liu, Y.H.; Langrock, A.; Zachariah, M.R.; Wang, C.S. Uniform nano-Sn/C composite anodes for lithium ion batteries. *Nano Lett.* **2013**, *13*, 470–474. [[CrossRef](#)]
39. Xia, Y.; Zheng, J.M.; Wang, C.M.; Gu, M. Designing principle for Ni-rich cathode materials with high energy density for practical applications. *Nano Energy* **2018**, *49*, 434–452. [[CrossRef](#)]
40. Chen, Y.; Niu, Y.; Tian, T.; Zhang, J.; Wang, Y.; Li, Y.; Qin, L.-C. Microbial reduction of graphene oxide by *Azotobacter chroococcum*. *Chem. Phys. Lett.* **2017**, *677*, 143–147. [[CrossRef](#)]
41. Li, O.L.; Chiba, S.; Wada, Y.; Panomsuwan, G.; Ishizaki, T. Synthesis of graphitic-N and amino-N in nitrogen-doped carbon via a solution plasma process and exploration of their synergic effect for advanced oxygen reduction reaction. *J. Mater. Chem. A* **2017**, *5*, 2073–2082. [[CrossRef](#)]
42. Peng, H.; Mo, Z.; Liao, S.; Liang, H.; Yang, L.; Luo, F.; Song, H.; Zhong, Y.; Zhang, B. High performance Fe-and N-doped carbon catalyst with graphene structure for oxygen reduction. *Sci. Rep.* **2013**, *3*, 1765. [[CrossRef](#)]
43. Mutuma, B.K.; Matsoso, B.J.; Momodu, D.; Oyedotun, K.O.; Coville, N.J.; Manyala, N. Deciphering the structural, textural, and electrochemical properties of activated BN-doped spherical carbons. *Nanomaterials* **2019**, *9*, 446. [[CrossRef](#)]
44. Lin, T.W.; Su, C.Y.; Zhang, X.Q.; Zhang, W.; Lee, Y.H.; Chu, C.W.; Lin, H.Y.; Chang, M.T.; Chen, F.R.; Li, L.J. Converting graphene oxide monolayers into boron carbonitride nanosheets by substitutional doping. *Small* **2012**, *8*, 1384–1391. [[CrossRef](#)]
45. Sunu, S.; Prabhu, E.; Jayaraman, V.; Gnanasekar, K.; Seshagiri, T.; Gnanasekaran, T. Electrical conductivity and gas sensing properties of MoO₃. *Sens. Actuators B Chem.* **2004**, *101*, 161–174. [[CrossRef](#)]
46. Wei, H.; Xi, Q.; Chen, X. a.; Guo, D.; Ding, F.; Yang, Z.; Wang, S.; Li, J.; Huang, S. Molybdenum carbide nanoparticles coated into the graphene wrapping n-doped porous carbon microspheres for highly efficient electrocatalytic hydrogen evolution both in acidic and alkaline media. *Adv. Sci.* **2018**, *5*, 1700733. [[CrossRef](#)]
47. Li, O.L.; Hayashi, H.; Ishizaki, T.; Saito, N. Enhancement of conductivity in nano carbon balls by the addition of carbon tetrachloride via room temperature solution plasma process. *RSC Adv.* **2016**, *6*, 51864–51870. [[CrossRef](#)]
48. Song, F.; Hu, X. Exfoliation of layered double hydroxides for enhanced oxygen evolution catalysis. *Nat. Commun.* **2014**, *5*, 1–9. [[CrossRef](#)]
49. Jung, S.; McCrory, C.C.; Ferrer, I.M.; Peters, J.C.; Jaramillo, T.F. Benchmarking nanoparticulate metal oxide electrocatalysts for the alkaline water oxidation reaction. *J. Mater. Chem. A* **2016**, *4*, 3068–3076. [[CrossRef](#)]
50. Lin, Y.; Tian, Z.; Zhang, L.; Ma, J.; Jiang, Z.; Deibert, B.J.; Ge, R.; Chen, L. Chromium-ruthenium oxide solid solution electrocatalyst for highly efficient oxygen evolution reaction in acidic media. *Nat. Commun.* **2019**, *10*, 1–13. [[CrossRef](#)]

51. Merki, D.; Vrabel, H.; Rovelli, L.; Fierro, S.; Hu, X. Fe, Co, and Ni ions promote the catalytic activity of amorphous molybdenum sulfide films for hydrogen evolution. *Chem. Sci.* **2012**, *3*, 2515–2525. [[CrossRef](#)]
52. Zhang, H.; Zheng, J.; Chao, Y.; Zhang, K.; Zhu, Z. Surface engineering of FeCo-based electrocatalysts supported on carbon paper by incorporating non-noble metals for water oxidation. *New J. Chem.* **2018**, *42*, 7254–7261. [[CrossRef](#)]

Publisher’s Note: MDPI stays neutral with regard to jurisdictional claims in published maps and institutional affiliations.



© 2020 by the authors. Licensee MDPI, Basel, Switzerland. This article is an open access article distributed under the terms and conditions of the Creative Commons Attribution (CC BY) license (<http://creativecommons.org/licenses/by/4.0/>).